



Contents lists available at ScienceDirect

Engineering

journal homepage: www.elsevier.com/locate/eng

Article

Tailoring Photonic-Engineered Textiles with Butterfly-Mimetic Tertiary Micro/Nano Architectures for Superior Passive Radiative Cooling

Hongyu Guo^a, Tianye Niu^a, Jianyong Yu^{a,b}, Xueli Wang^{a,b,*}, Yang Si^{a,b,*}

^aState Key Laboratory for Modification of Chemical Fibers and Polymer Materials, College of Textiles, Donghua University, Shanghai 201620, China

^bInnovation Center for Textile Science and Technology, Donghua University, Shanghai 201620, China

ARTICLE INFO

Article history:

Available online xxxx

Keywords:

Biomimetic materials
Personal thermal management
Textiles
Passive radiative cooling

ABSTRACT

People could potentially mitigate heat discomfort when outdoors by combining passive radiative cooling (PRC) strategies with personal thermal management techniques. However, most current PRC materials lack wearing comfort and durability. In this study, a microarray technique is applied to fabricate the tailoring photonic-engineered textiles with intriguing PRC capability and appealing wearability. The developed radiative cooling textiles (RCTs) demonstrate appropriate air–moisture permeability, structural stability, and extended spectroscopic response with high sunlight reflectivity (91.7%) and robust heat emissivity (95.8%) through the atmospheric transparent spectral window. In a hot outdoor cooling test, a skin simulator covered by the RCTs displays a temperature drop of ~ 4.4 °C at noon compared with cotton textiles. The evolution of our mimetic structures may provide new insights into the generation of wearable, thermal–wet comfortable, and robust textiles for exploring PRC techniques in personal thermal management applications.

© 2023 THE AUTHORS. Published by Elsevier LTD on behalf of Chinese Academy of Engineering and Higher Education Press Limited Company. This is an open access article under the CC BY-NC-ND license (<http://creativecommons.org/licenses/by-nc-nd/4.0/>).

1. Introduction

With global warming, heat waves are occurring more frequently and with greater intensity [1]. Approximately a third of the global population is already exposed to conditions that involve necessary outdoor physical activities and industrial operations, leading to heat stress [2,3]. Heat stress not only has physiological and psychological consequences, but also diminishes industrial worker productivity, and in extreme cases, results in immeasurable suffering and loss of life [4]. Hence, personal thermal management (PTM)—a strategy that could efficiently regulate the body's microclimate to ensure thermal comfort in outdoor conditions, is critical [5,6]. Active cooling methods are prevalently employed for PTM, which primarily relies on a bulky compression cooling system that consumes substantial amounts of energy and requires access to electricity. A solution to these challenges, however, lies in passive radiative cooling (PRC), which achieves spontaneously cooling through the spectral responsiveness of materials [7]. Although recent research has yielded various PRC material designs of PRC materials, including metamaterials [8,9], multilayer dielectrics

[10–12], porous media [13–16], and their composites [17,18], there is still much work to be done. The majority of these materials lack flexibility, exhibit weak air–moisture permeability, and possess inadequate durability, rendering them unsuitable for direct use in PTM [6]. Therefore, it is highly important to produce a flexible PRC material with outstanding wearability for regulating the microclimate of the human body in outdoor settings [19–21].

A systematic design of the PRC textiles requires the optimization of two important characteristics: high sunlight reflectivity (R_{Solar} ; the wavelength (λ) of 0.3–2.5 μm) [22,23] and strong heat emissivity through the atmospheric transparent spectral window ($\varepsilon_{\text{ATSW}}$; λ of 8–13 μm) [24–27]. Meeting the two of these requirements with a single component remains a significant challenge, necessitating the construction of multi-layer composite structures [28–30]. Therefore, the hierarchical woven fabrics and multi-layer nanofibrous membranes [31–34], which have acceptable optical properties and adequate PRC properties, make up the majority of the recently disclosed PRC materials for PTM. However, two issues hindered the practical use of cutting-edge PRC textiles: ①The stacking of multi-layer structures reduces the textiles' air–moisture permeability, making them less comfortable to wear and causing sweat to condense; and ②the weak bonding fastness between the layers of textiles makes it prone to separation during washing and prolonged wearing, resulting in poor durability. We concluded

* Corresponding authors.

E-mail addresses: wxl@dhu.edu.cn (X. Wang), yangsi@dhu.edu.cn (Y. Si).

<https://doi.org/10.1016/j.eng.2023.07.019>

2095-8099/© 2023 THE AUTHORS. Published by Elsevier LTD on behalf of Chinese Academy of Engineering and Higher Education Press Limited Company.

This is an open access article under the CC BY-NC-ND license (<http://creativecommons.org/licenses/by-nc-nd/4.0/>).

that the predicted answer to these issues is the deliberate development of monolayer PRC textiles. For this principle, we investigated the reported PRC features and were significantly enlightened by the monolayer wing with the fascinating photonic structure of the *Sericanus montelus* (*S. montelus*); due to its delicate hierarchical porous structures and intrinsic material characteristics, the wing has a broadband sunlight reflection and great heat dissipation through the atmospheric transparent spectral window (ATSW) [35–39]. We thus reason that constructing butterfly-mimetic monolayer PRC textiles using high mid-infrared (MIR) emittance materials holds great promise for achieving superior PRC properties and wearability in outdoor settings.

Herein, we present a microarray technology to develop tailoring photonic-engineered textiles with butterfly-mimetic structures for effective personal outdoor PRC. An ideal extended spectroscopic response (λ of 0.3–13 μm) is directly provided by the fine tertiary micro/nano structures. The monolayer textiles with through-holes offer gas and water transport channels, ensuring adequate air-moisture permeability while maintaining structural stability. Thus, the resulting radiative cooling textiles (RCTs) exhibit the integrated properties of ideal extended spectroscopic response (R_{solar} of 91.7% and $\varepsilon_{\text{ATSW}}$ of 95.8%), desirable air permeability, adequate water vapor transmittance, and structural robustness, which are promising candidates for exploring PRC techniques in PTM applications.

2. Material and methods

2.1. Materials

Polyester (PET) textile was purchased from Gaoyi Yongsheng Textile Co., Ltd. (China). Cellulose triacetate (CTA; polymer), isopropanol, and ammonia were provided by Shanghai Aladdin Biochemical Technology Co., Ltd. (China). CH_2Cl_2 and bromoform were purchased from Shanghai Macklin Biochemical Co., Ltd. (China). SiO_2 nanoparticles (NPs) were provided by Jingjiang Tonggao Chemical Co., Ltd. (China). Specimen of *S. montelus* was provided by Shanghai Qiuyu Biotechnology Co., Ltd. (China).

2.2. Preparation of RCTs

We first introduced SiO_2 NPs to the water in a predetermined quantity (0.5 wt%) and ultrasonically dispersed them for 4 h. Then, the PET textile was immersed in the SiO_2 NPs dispersion liquid before being stirred and dried. The textile was then completely immersed in the CTA solution (2.3 wt%) in CH_2Cl_2 , and pressure was then applied to drive the liquid into the aperture gap of the textiles. After 30 min, it was quickly transferred to a static humidity (75% \pm 2%) environment constructed with a saturated sodium chloride solution. Breath figures formed when moisture touched the cool substrate. After the solvent and condensed water have completely evaporated, orderly homogenous pores are created on the surface.

2.3. Characterization

Xenon lamp (CEL-HXF300-T3; Shanghai Liyi Biotechnology, China) was used to test the cooling performance of *S. montelus*. Scanning electron microscopy (SEM; VEGA 3 LMU; Tescan, Czech Republic) was used to examine the morphology. The finite-difference time-domain (FDTD) was used to simulate the optical properties of different structures. Ultraviolet (UV)–visible (Vis)–near infrared (NIR) spectrophotometer (UV3600 PLUS; Shimadzu, Japan) and the Fourier transform infrared spectrometer (NEXUS-670; Thermo Fisher Scientific, USA) were used to determine the optical properties. A homemade test box was used to test direct

thermal measurements (Supplementary method in Appendix A). A one-dimensional steady-state heat transfer model (Supplementary method in Appendix A) was carried out to calculate the cooling demand of different textiles. A tensile tester (HD026N-300; Nantong Hongda, China) was used to analyze the tensile strength and elongation. To demonstrate the softness of the RCTs, we conducted the bending rigidity tests on the bending rigidity tester (LLY-01; Laizhou Electronic, China). The water vapor transmission (WVT) rate was determined using a textile moisture permeability testing device (YG601H; Ningbo Textile Instrument, China), the air permeability was determined using an air-permeability tester (YG461E; Dongguan Bolade, China), and the hydrophilicity was tested by the contact angle tester (SL150; KINO, USA). The infrared thermal images were taken with an infrared camera (315; FOTRIC, China). The Martindale abrasion tester (YG401-6; Shaanxi Changling Textile, China), washing machine (Y089D; Wenzhou Fangyuan, China), and Dynamic mechanical analysis (Q850; TA, USA) were used to investigate the durability of the textiles.

3. Results and discussion

3.1. Biomimetic structure design and fabrication

S. montelus, a butterfly species that lives in East Asia, has two seasonal morphs with fascinating PRC functions for individual thermal regulation [35,40,41]. Due to the carefully constructed hierarchical pores on the wing scale, *S. montelus* exhibits structural whiteness with broadband sunlight reflectance (Fig. 1(a)). After 30 min of xenon lamp irradiating (700 $\text{W}\cdot\text{m}^{-2}$), the temperature differential (ΔT) between the two regions (white and black) of the wing reached ~ 8.7 $^\circ\text{C}$, indicating the high sunlight reflectivity of the white parts (Fig. S1(a) in Appendix A). Simultaneously, as illustrated in Fig. S1(b) in Appendix A, we discovered that the wing scale changed from being opaque structurally to almost transparent when it was submerged in the bromoform (a liquid that matches the index of chitin). These findings suggested that the wing's peculiar microstructure, known as structural whiteness, is responsible for its broad spectrum reflectance. Furthermore, SEM was used to explore the microstructures of the wing scale at several angles. As represented in Fig. 1(a) and Fig. S2 in Appendix A, the delicate hierarchical porous structure of the wing scale contained bulges with multiple arrayed micro-pores, raised ridges that run parallel to the pedestal, and grooves that were arranged alongside the ridges. Meanwhile, benefiting from the major component (chitin) of the wing scale with high MIR-absorbance, the wing exhibited high emissivity in ATSW [33]. Taking inspiration from this fascinating natural photonic structure, we designed monolayer PRC textiles based on three criteria: ①The textiles must be able to effectively reflect sunlight that reduces solar energy gain; ②the textiles must be high emittance through ATSW that evaluates radiative heat loss; ③the textiles should possess high air-moisture permeability and structural stability. The first two requirements are satisfied by constructing delicate tertiary micro/nano architectures with strong Mie's scattering and multiple reflections using high $\varepsilon_{\text{ATSW}}$ materials (CTA and SiO_2 NPs) [23], which were illustrated to be high MIR absorption/emission materials due to the vibration of C–O bonds [6,27] and Si–O bonds [21]. To fulfill the third criterion, we successfully assembled the surface of the tailoring microstructure by microarray technique to robustly embed fine photonic architectures into textiles.

As demonstrated in Fig. 1(b), RCTs were fabricated using the static breath figure patterning method, a microarray technique (Supplementary method in Appendix A). The microarray technique started with immersion and ultrasonic of commercial twill PET textiles in SiO_2 NPs dispersion. Upon drying in air, the dried

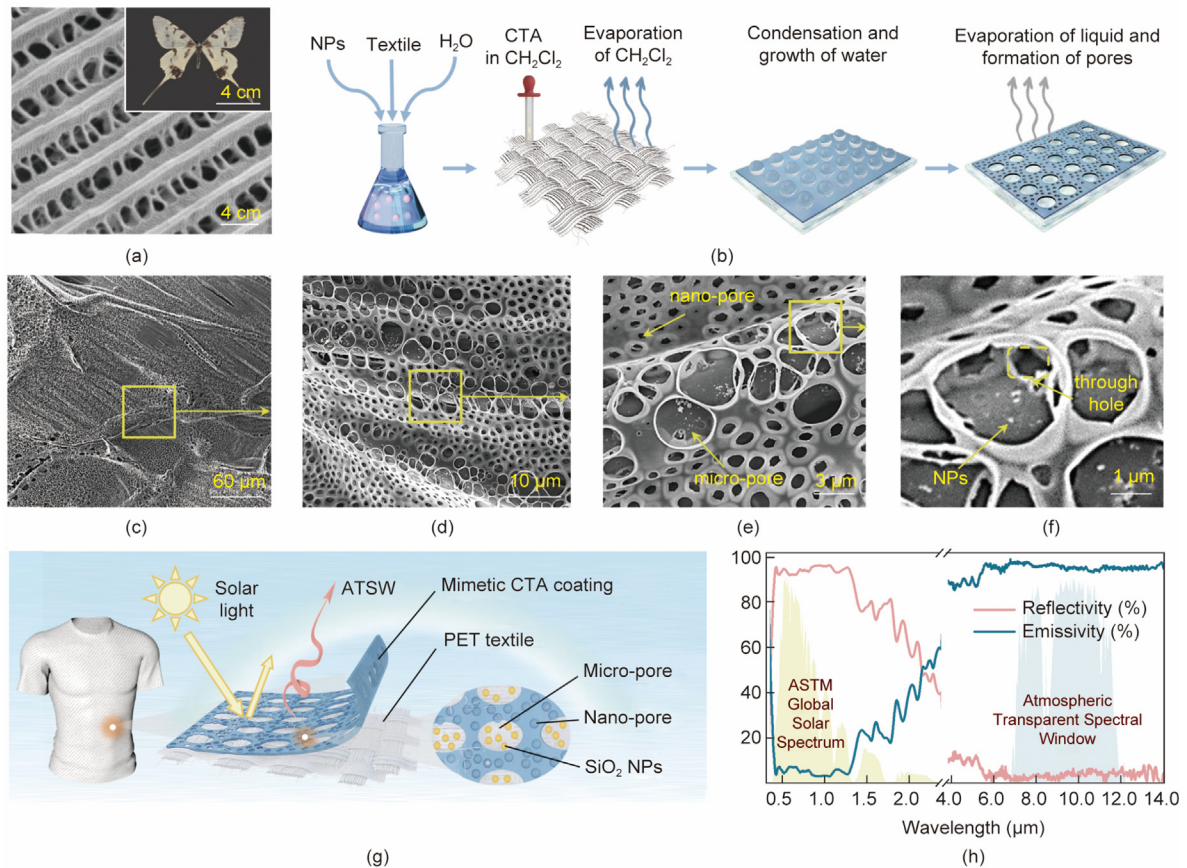


Fig. 1. (a) SEM image of *S. montelus*' wing. The insert shows a photograph of *S. montelus*. (b) Schematic illustration of the preparation process of the RCTs. (c–f) Morphologies of RCTs with tertiary micro/nano architectures at different magnifications. (g) Schematic illustration of the working principle of the RCTs. (h) Spectral reflectivity and emissivity of the RCTs against normalized American society for testing and materials (ASTM) 1.5 global solar spectrum and the ATSW transmissivity, respectively.

PET–SiO₂ textiles were fully soaked into the prefabricated CTA casting solution, and pressure was applied to impose the liquid into the aperture gap of the textiles (Fig. S3 in Appendix A). After 30 min, the textile was quickly moved to a static high-humidity environment. The evaporation of the volatile dissolvent (CH₂Cl₂), which encourages the condensation and expansion of water droplets, is to blame for a considerable drop in surface temperature. The ΔT between the substrate surface and the droplets gradually diminished and finally disappeared once the substrate surface was entirely covered by the droplets. After the evaporation of CH₂Cl₂ and condensed water, the film finally formed with arranged pore arrays using droplets as a template. Eventually, the bio-inspired tertiary micro/nano architectures formed on the PET textiles, which contain the micro-pores (with an average diameter (d_{avg}) of 2.84 μm) arranged on the fibers, nano-pores (d_{avg} of 586 nm) ordered between the fibers, and SiO₂ NPs (d_{avg} of 165 nm) randomly distributed throughout the textile structures (Figs. 1(c)–(f)). The resulting textiles with a thickness of (582 \pm 51) μm presented a desirable extended spectroscopic response (R_{solar} of 91.7% and ϵ_{ATSW} of 95.8%) benefiting from the tailoring photonic structure, which could effectively lower the solar energy absorption and evaluate the heat emission to the outer space through ATSW (Figs. 1(g) and (h)). The photographs of the RCTs, untreated PET textiles, and commercial cotton textiles for comparison were shown in Fig. S4 in Appendix A.

3.2. Optical performance optimization

To promote the PRC properties of the textiles by multi-level structural design and material selection [6], we simulated the

optical parameter of the tailoring structures (Fig. 2(a) and Supplementary method in Appendix A). Over the wavelength of 0.3–2.5 μm , a material could substantially scatter the light wave with a wavelength near the diameter of the components (particle or pore size) according to Mie's scattering theory [23]. To forecast the scattering ability of the dielectric particles based on their refractive index, the FDTD method was used (Fig. S5 in Appendix A). We estimated and demonstrated that the SiO₂ NPs with a particle size of 200 nm could scatter most of the sunlight over the wavelengths of 0.3–0.55 μm . Analogously, the scattering property between 0.55 and 2.5 μm was also simulated by evenly distributing holes of various sizes on a 4 μm \times 4 μm \times 2 μm CTA pedestal. Since the scattering ability of different apertures varies with wavelength, we proved that the apertures of 0.6 and 3.0 μm could efficiently scatter the Vis and NIR light, respectively. Furthermore, CTA and SiO₂ were illustrated to be high MIR absorption/emission materials due to the vibration of C–O bonds [6,27] and Si–O bonds [21], which could cooperate to enhance the heat exchange with the cold outer space through ATSW.

By varying the forming temperature and CTA concentration, we explored the pore size fluctuation in order to accurately build the optimal structure (Fig. 2(b), Fig. S6, and Supplementary discussion in Appendix A). It is interesting to note that, in contrast to earlier studies [42,43], our material had a multi-level porous structure caused by the unevenness of the textile surface. The forming schematic diagram shown in Fig. 2(c) and Supplementary discussion in Appendix A indicated that the shallow thickness of the CTA solution on the top of fibers (blue arrows) resulted in faster evaporation rates of CH₂Cl₂ and an earlier emergence of water droplet templates. Thus, with early condensation and longer growth times

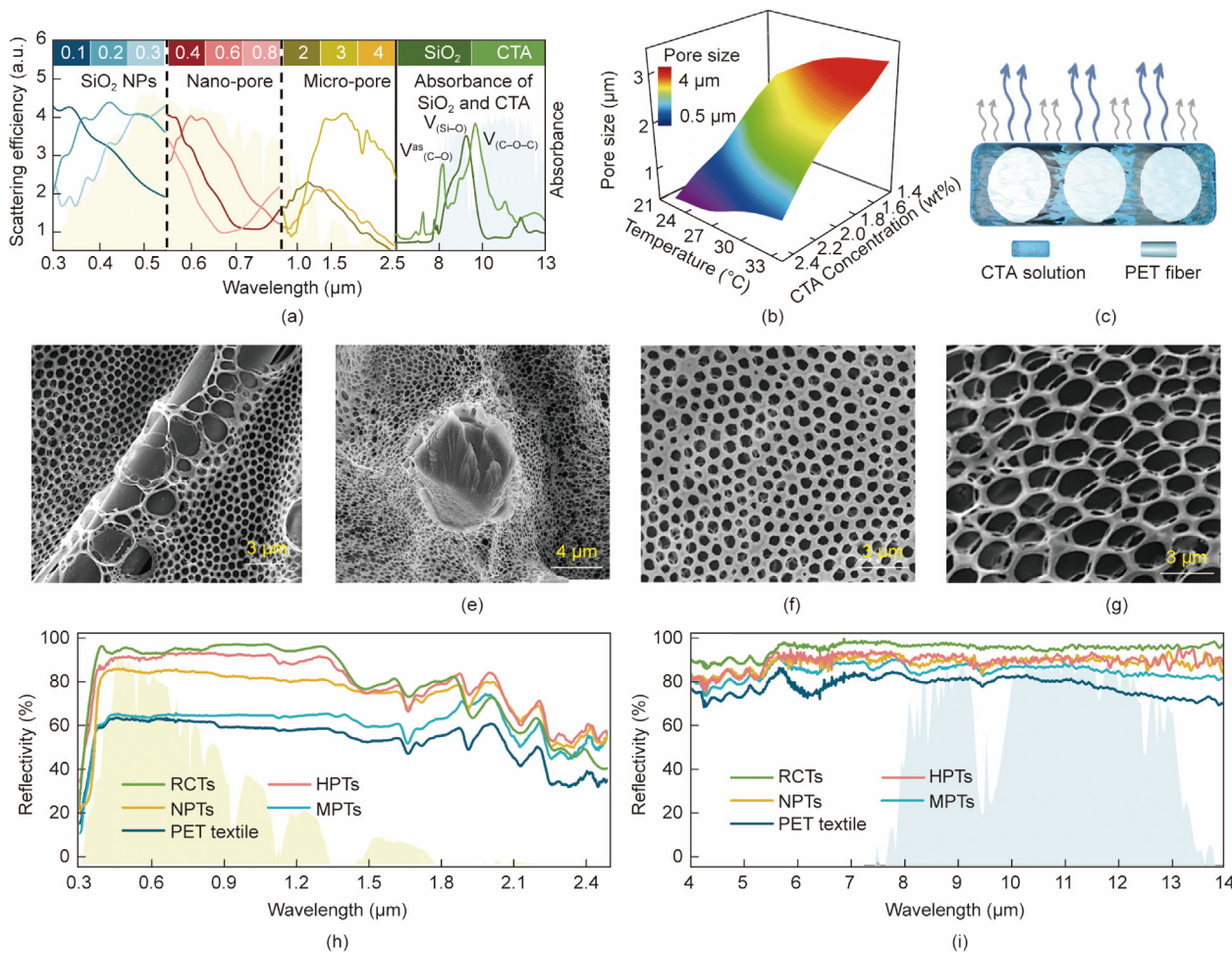


Fig. 2. (a) Simulated scattering efficiency of microstructure (SiO₂ NPs, nano-pores, and micro-pores) and MIR absorbance of CTA and SiO₂. (b) Relationship between the average pore size and the formation parameters (temperature and CTA concentration). (c) Forming mechanism schematic of the hierarchical porous structure. (d) SEM image of the HPTs. (e) Cross-sectional SEM image of the HPTs. (f) SEM image of the NPTs. (g) SEM image of the MPTs. (h) Spectral reflectivity against normalized ASTM 1.5 global solar spectrum. (i) Spectral emissivity against the ATSW transmissivity.

of water droplets, the micro-pores formed orderly on the top of each fiber. On the contrary, the slower evaporation rate of CH₂Cl₂ between the fibers enabled the formation of several layers of nano-pores (Figs. 2(d) and (e), and Fig. S7 in Appendix A). As illustrated in Figs. 2(f) and (g), and Fig. S8 in Appendix A, we also constructed orderly homogenous pores with average apertures of 0.53–3.21 μm on the textiles. In the meanwhile, by adjusting the preparation settings, we were able to regulate the CTA coverage area and SiO₂ concentrations (Figs. S9 and S10, and Supplementary discussion in Appendix A). The optical properties of the different porous structural textiles were illustrated in Figs. 2(h) and (i), and Fig. S11 in Appendix A, namely RCTs, hierarchical porous textiles (HPTs), homogenous nano-porous textiles (NPTs), homogeneous micro-porous textiles (MPTs), and untreated PET textiles. Due to full spectrum Mie's scattering and multiple reflections, the RCTs exhibited a R_{solar} of 91.7%, whereas the R_{solar} of HPTs marginally decreased to 88.7%, especially in the UV-Vis wavelength region, as a result of the absence of SiO₂ NPs. For the textiles with homogeneous porous CTA, the R_{solar} of NPTs falls to 81.2%, whereas the R_{solar} of MPTs drastically decreases in the UV-Vis wavelength band due to the monolayer micro-porous structure. Moreover, in order to further clarify the reasons for the increase in reflectivity, we normalized the reflectance results against the weight and thickness of the PET substrates (Supplementary discussion, Fig. S12, and Table S1 in Appendix A). According to the emission

spectra, all five textiles exhibited high thermal emittances through the ATSW. The ATSW emissivity rises from 80.2% to 95.8% with the addition of CTA and SiO₂ NPs, demonstrating that the intrinsic characteristics of the materials had a greater impact on $\varepsilon_{\text{ATSW}}$.

3.3. Spectrum response mechanism analysis

Numerically, we analyzed the relationship between microstructure and optical properties to infer the mechanism of the desired spectrum response. The wing scale of *S. montelus* presented broadband sunlight reflectance, which is attributed to the delicate hierarchical porous structure of the wing scale contains bulges with numerous arrayed micro-pores (d_{avg} of 1.81 μm), raised ridges that run parallel to the pedestal, and grooves that are arranged alongside the ridges (d_{avg} of 0.17 μm). Similarly, the pore diameters of the RCTs, which had a bimodal distribution centered between 0.6 and 2.8 μm, suggest that a comparable optical mechanism may exist (Fig. 3(a)). The FDTD simulation began with the simplified three-dimensional (3D) model constructions of the wing scale and RCTs as shown in Figs. 3(b) and (c), originating from the SEM image (Fig. S13(a) in Appendix A). As shown in Figs. S13(b) and (c) in Appendix A, the CTA porous structures had been fabricated on the surface of PET fibers with the micro-pores and the nano-pores. As corroborated by the simulated optical parameters, the pedestal possessed the same width as that of a wing scale's groove

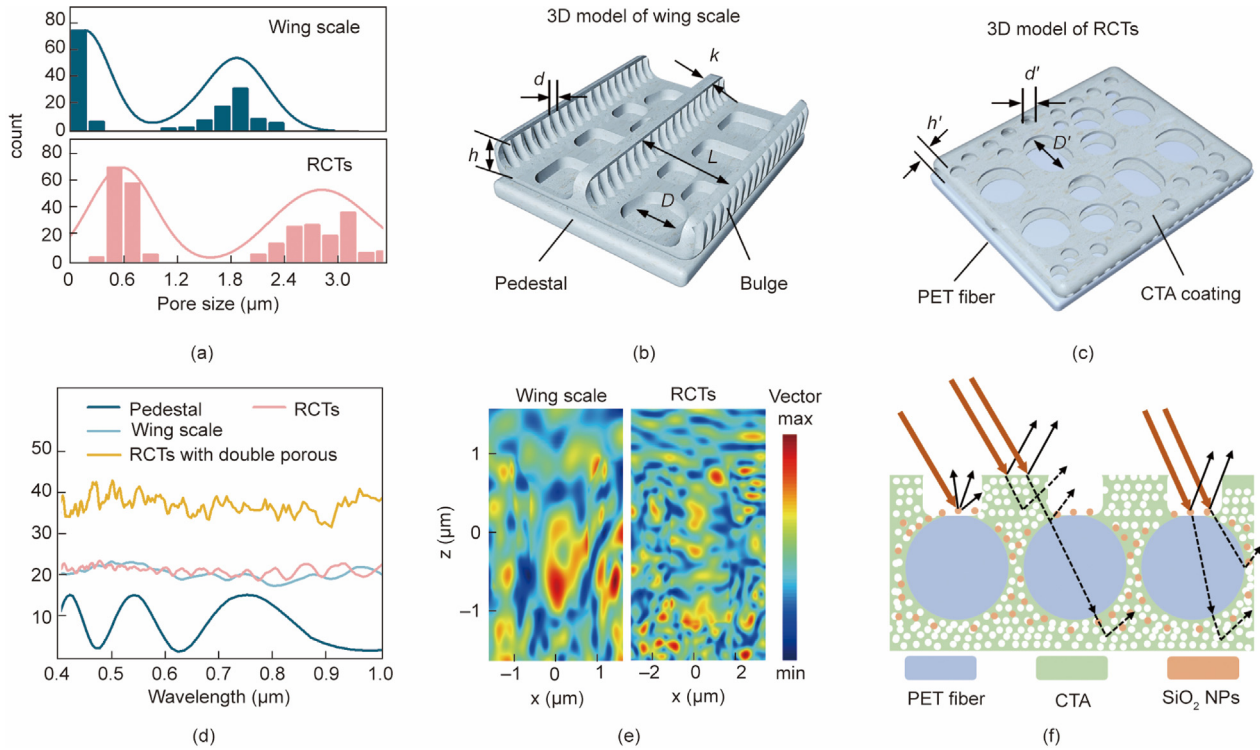


Fig. 3. (a) Pore size distributions of the wing scale and the RCTs. (b) Simplified 3D simulation model of the wing scale of *S. montelus*, h : thickness of ridge; D : diameter of micro-pores; d : width of nano-pores; L : width of the grooves; k : width of ridge. (c) Simplified 3D simulation model of the RCTs, h' : thickness of CTA; D' : diameter of micro-pores; d' : diameter of nano-pores. (d) Simulated spectra reflectivity of different structures. (e) The distribution of Poynting vectors on cross sections of wing scale and RCTs under 700 nm. (f) Reflectance mechanism schematic of the RCTs.

(L), which showed a weak reflectance during the wavelength between 0.4 and 1 μm. Due to multiple scattering, the reflectance dramatically increased to more than 20% with the introduction of the bulge structures, while the reflectance of RCTs with a double porous structure also increased to ~36% (Fig. 3(d)). In order to visually observe the scattering of light, we presented the simulated Poynting vectors of the two structural models under the incident light (λ of 700 nm). Poynting vector, which represents the energy flux density vector in the electromagnetic field, indicates the energy passing through the vertical unit area per unit of time [35]. As shown in Fig. 3(e), the Poynting vector of our RCTs showed more erratic and abundant hotspots than that of the wing scale, which indicated a more dispersive scattering direction of light. Based on our characteristics of the microstructures and calculations of the optical properties, we presented our assumption of the reflectance mechanism of RCTs in Fig. 3(f) and Fig. S13(b) in Appendix A. The hierarchical pores of RCTs yield a broad spectrum of apertures, leading to pronounced Mie's scattering; while the abundant longitudinal nanopore configurations and SiO₂ nanoparticles within the substance engender multiple light reflections. Consequently, the RCTs demonstrate exceptional sunlight reflectivity.

3.4. Direct cooling performance and wearability

To estimate the direct radiative cooling performance of the RCTs, we carried out a continuous outdoor measurement of temperature and cooling demand (CD) under a clear sky in Shanghai, China on the 5th and 10th of August, 2022. As shown in Fig. 4(a), Fig. S14 and Supplementary method in Appendix A, the RCTs were placed in a homemade device elevated to a height above the ground of 0.7 m to lessen the effects of thermal convection and conduction during the direct cooling experiment (Supplementary method in Appendix A), we also tested the sun intensity with a

pyranometer. Promisingly, under a relative humidity of 38% and average solar irradiance intensity of approximately 810 W·m⁻² at noon, the ΔT of the simulator surface covered by RCTs reached approximately 4.4, 3.5, and 2.0 °C compared with that of the commercial cotton textiles, PET textiles, and ambient respectively during peak sun irradiation between 11:00 and 15:00 (Fig. 4(b)). As a result, the CD of RCTs was about 174 W·m⁻² less than cotton. The increased value of CD implied that additional cooling energy was necessary to uphold a steady body temperature of 34 °C in human beings, indicating improved thermal comfort in hot outdoor environments. Meanwhile, during the cooling test of a whole day, the average temperature drop reached 2.8 °C (Fig. 4(c)). Therefore, our RCTs possessed an adequate cooling performance, which was comparable with that of the previously reported textiles [6,27]. Moreover, we assessed the temperatures of the body surface covered by RCTs and cotton textiles using an infrared thermal imager. The ΔT reached approximately 2.8 °C after 30 min of sun exposure, demonstrating the cooling properties in practical wearing situations (Fig. 4(d)).

RCTs have great wearability in addition to their desirable cooling capabilities, which was important for direct application to PTM. Mechanical testing revealed that our RCTs could withstand a tensile stress of 1158 N and a strain of 11%, which was significantly better than those of cotton textiles, as shown in Fig. 4(e). The swelling of the original fiber would be the cause of the decrease in strength and elongation, and the overall material felt slightly hard after treatment. To further test the comfortability of RCTs, we conducted an air permeability test, which was a measurement of the capacity to permit air to pass when a specific pressure is applied. Under the pressure drop of 100 Pa, the air permeability of the RCTs (grammage of (221.7 ± 11.6) g·m⁻², the thickness of (582 ± 51) μm), untreated PET textiles (grammage of (214.5 ± 5.4) g·m⁻², the thickness of (531 ± 16) μm), and cotton textiles (grammage of (201.9 ± 2.1) g·m⁻², the thickness of (481 ± 32) μm) were 45.3, 47.3, 49.1 mm·s⁻¹,

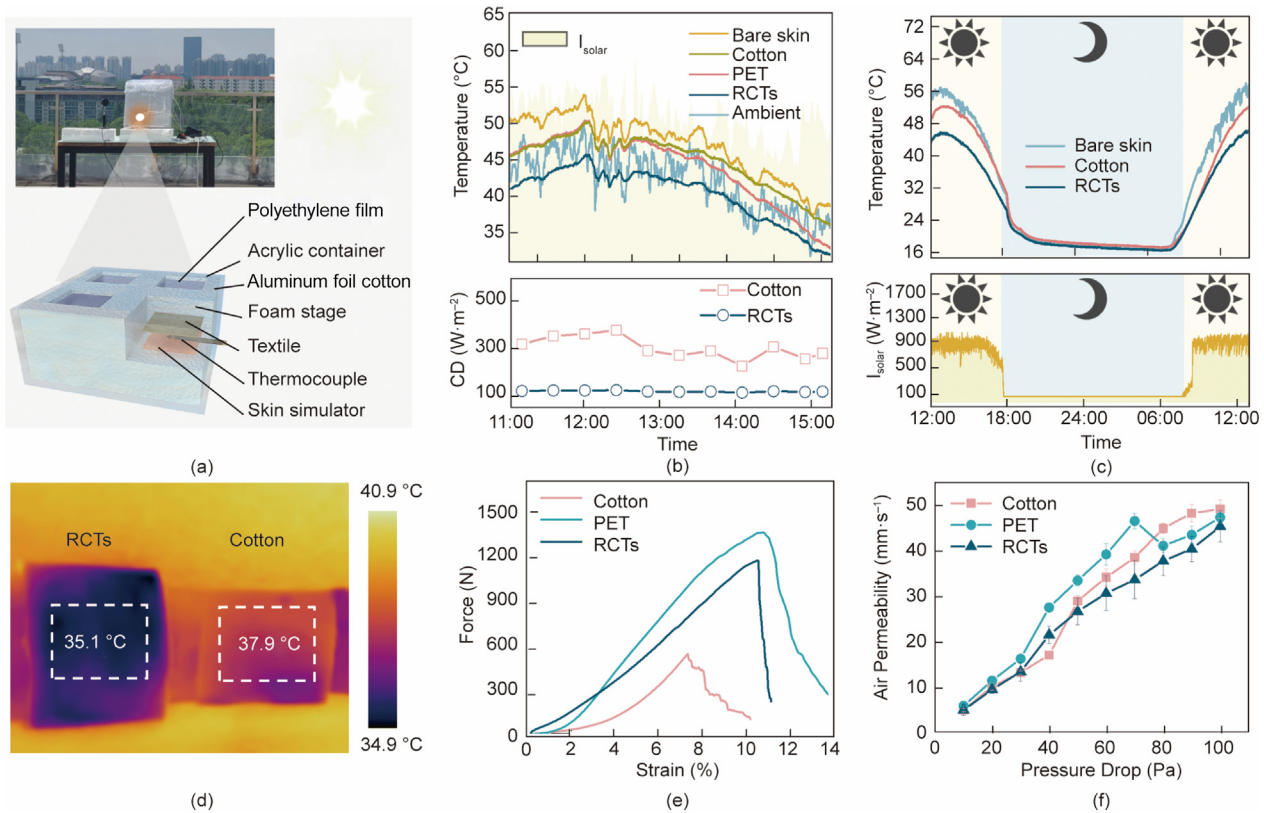


Fig. 4. (a) A photo and a schematic of the homemade thermal measurement apparatus used to assess the practical radiative cooling properties. (b) The temperature and CD of skin simulators in the same location under different textiles from 11:00 to 15:00. (c) The temperature and solar radiation intensity of the 24 h continuous measurement. (d) Infrared thermal image of human skin covered by RCTs and commercial cotton textiles after 30 min of exposure to direct sunlight. (e) Mechanical measurement of textiles. (f) Air permeability of textiles.

respectively, as shown in Fig. 4(f). Meanwhile, the WVT rate of the RCTs was $4744 \text{ g}\cdot\text{m}^{-2}\cdot\text{d}^{-1}$, indicating little sweat condensation and great moisture comfortability (Fig. S15 in Appendix A). Furthermore, we conducted the moisture absorption test, water resistance experiment, and contact angle measurements on RCTs, untreated PET textiles, and cotton textiles to further demonstrate the wearability of our materials (Figs. S16, S17, and Supplementary discussion in Appendix A). Besides, softness was a key factor for the wearability and comfortability of radiative cooling textiles. As shown in Fig. S18(a) and (b) in Appendix A, the bending rigidity of the RCTs, untreated textiles, and cotton textiles was 10.6, 8.1, and 2.7 mN·cm, respectively. The softness of RCTs was lower than that of untreated PET textiles due to the porous structure filled between the fibers and yarns, but RCTs could still be twisted with fundamental wearable potential (Fig. S17(c) in Appendix A).

The importance of durability is often underestimated, yet durability remains a crucial requirement for PRC textiles. To test the durability of the RCTs, we performed abrasion resistance testing on the Martindale abrasion tester, as shown in Fig. S19 in Appendix A [19]. Compared with untreated PET and cotton textiles, the RCTs showed even better resistance to abrasion, which was demonstrated by the lower mass reduction of 2.15% and undetectable surface damage. The mass reduction of RCTs was on account of the slight destruction of tertiary architectures. Attributed to the strong interfacial adhesion of PET and CTA, the CTA film critically reduced the frictional force on the single fiber during abrasion and effectively inhibited the extraction of fibers from yarn/textile structures. Furthermore, we measured the R_{solar} and $\varepsilon_{\text{ATSW}}$ of RCTs after 10 000 abrasion cycles to further demonstrate the abrasion resistance (Fig. S20 in Appendix A). Because of the slight destruction of tertiary architectures, the R_{solar} and $\varepsilon_{\text{ATSW}}$ were decreased

by 6.3% and 3.3%, respectively. In addition, the mass of RCTs was slightly decreased by 1.2%, while the R_{solar} and $\varepsilon_{\text{ATSW}}$ exhibited almost no degradation after 10 000 bending cycles (Figs. S21 and S22 in Appendix A). The RCTs showed excellent bending resistance because of the adequate tenacity and bending recovery of CTA. Moreover, after 50 washing cycles, the mass of RCTs decreased by 1.9%, while the R_{solar} and $\varepsilon_{\text{ATSW}}$ decreased by 8.9% and 2.7% respectively (Figs. S23 and S24 in Appendix A). When compared to those of cutting-edged PRC textiles, which were considered to be promising candidates for exploring PRC in temperature-regulating wearable applications, RCTs offered the appropriate passive radiative cooling ability and wearability.

4. Conclusions

In summary, we developed a facile and adaptable pathway for the fabrication of photonic-engineered PRC textiles via the microarray technique. The tailoring tertiary micro/nano architectures of the resulting textiles endowed excellent extended spectroscopic response (R_{solar} of 91.7% and $\varepsilon_{\text{ATSW}}$ of 95.8%) which yields a temperature drop of approximately $4.4 \text{ }^{\circ}\text{C}$ compared to the commercial cotton textiles in the practical cooling properties measurement. Additionally, the robust monolayer design with a through-hole structure of RCTs provided channels for the transport of air and moisture, leading to a desirable air permeability of $45.3 \text{ mm}\cdot\text{s}^{-1}$ and water vapor transmittance of $4744 \text{ g}\cdot\text{m}^{-2}\cdot\text{d}^{-1}$, while preserving structural stability and facile service. Our biomimetic design and the development of the monolayer photonic-engineered textiles provided a versatile platform for exploring

PRC materials in personal thermal management applications for personal thermal control that effectively save energy.

Acknowledgments

This work was supported by the Ministry of Industry and Information Technology, the National Development and Reform Commission of the Peoples Republic of China, the Fundamental Research Funds for the Central Universities (2232020A-06), the Science and Technology Commission of Shanghai Municipality (20QA1400500, 21130750100, and 22dz1200102), and Huo Yingdong Education Foundation (171065).

Compliance with ethics guidelines

Hongyu Guo, Tianye Niu, Jianyong Yu, Xueli Wang, and Yang Si declare that they have no conflict of interest or financial conflicts to disclose.

Appendix A. Supplementary material

Supplementary data to this article can be found online at <https://doi.org/10.1016/j.eng.2023.07.019>.

References

- Jacox MG, Alexander MA, Amaya D, Becker E, Bograd SJ, Brodie S, et al. Global seasonal forecasts of marine heatwaves. *Nature* 2022;604(7906):486–90.
- Pennisi E. Living with heat. *Science* 2020;370(6518):778–81.
- Chen B, Xie MM, Feng QQ, Wu RR, Jiang L. Diurnal heat exposure risk mapping and related governance zoning: a case study of Beijing. *China Sustain Cities Soc* 2022;81:103831.
- How V, Singh S, Dang T, Fang Lee L, Guo HR. The effects of heat exposure on tropical farm workers in Malaysia: six-month physiological health monitoring. *Int J Environ Health Res* 2023;33(4):413–29.
- Hsu PC, Song AY, Catrysse PB, Liu C, Peng Y, Xie J, et al. Radiative human body cooling by nanoporous polyethylene textile. *Science* 2016;353(6303):1019–23.
- Zeng S, Pian S, Su M, Wang Z, Wu M, Liu X, et al. Hierarchical-morphology metafabric for scalable passive daytime radiative cooling. *Science* 2021;373(6555):692–6.
- Cai L, Song AY, Li W, Hsu PC, Lin D, Catrysse PB, et al. Spectrally selective nanocomposite textile for outdoor personal cooling. *Adv Mater* 2018;30(35):e1802152.
- Li T, Zhai Y, He S, Gan W, Wei Z, Heidarinejad M, et al. A radiative cooling structural material. *Science* 2019;364(6442):760–3.
- Tang K, Dong K, Li J, Gordon MP, Reichertz FG, Kim H, et al. Temperature-adaptive radiative coating for all-season household thermal regulation. *Science* 2021;374(6574):1504–9.
- Kim M, Lee D, Son S, Yang Y, Lee H, Rho J. Visibly transparent radiative cooler under direct sunlight. *Adv Opt Mater* 2021;9(13):2002226.
- So S, Yang Y, Son S, Lee D, Chae D, Lee H, et al. Highly suppressed solar absorption in a daytime radiative cooler designed by genetic algorithm. *Nanophotonics* 2022;11(9):2107–15.
- Raman AP, Anoma MA, Zhu L, Rephaeli E, Fan S. Passive radiative cooling below ambient air temperature under direct sunlight. *Nature* 2014;515(7528):540–4.
- Lee D, Go M, Son S, Kim M, Badloe T, Lee H, et al. Sub-ambient daytime radiative cooling by silica-coated porous anodic aluminum oxide. *Nano Energy* 2021;79:105426.
- Mandal J, Jia MX, Overvig A, Fu YK, Che E, Yu NF, et al. Porous polymers with switchable optical transmittance for optical and thermal regulation. *Joule* 2019;3(12):3088–99.
- Mandal J, Fu Y, Overvig AC, Jia M, Sun K, Shi NN, et al. Hierarchically porous polymer coatings for highly efficient passive daytime radiative cooling. *Science* 2018;362(6412):315–9.
- Li D, Liu X, Li W, Lin Z, Zhu B, Li Z, et al. Scalable and hierarchically designed polymer film as a selective thermal emitter for high-performance all-day radiative cooling. *Nat Nanotechnol* 2021;16(2):153–8.
- Zhai Y, Ma YG, David SN, Zhao DL, Lou RN, Tan G, et al. Scalable-manufactured randomized glass-polymer hybrid metamaterial for daytime radiative cooling. *Science* 2017;355(6329):1062–6.
- Li PL, Wang A, Fan JJ, Kang Q, Jiang PK, Bao H, et al. Thermo-optically designed scalable photonic films with high thermal conductivity for subambient and above-ambient radiative cooling. *Adv Funct Mater* 2022;32(5):2109542.
- Alberghini M, Hong S, Lozano LM, Korolovych V, Huang Y, Signorato F, et al. Sustainable polyethylene fabrics with engineered moisture transport for passive cooling. *Nat Sustain* 2021;4(8):715–24.
- Peng YC, Chen J, Song AY, Catrysse PB, Hsu PC, Cai LL, et al. Nanoporous polyethylene microfibres for large-scale radiative cooling fabric. *Nat Sustain* 2018;1(2):105–12.
- Zhang X, Yang W, Shao Z, Li Y, Su Y, Zhang Q, et al. A moisture-wicking passive radiative cooling hierarchical metafabric. *ACS Nano* 2022;16(2):2188–97.
- Chae D, Lim H, So S, Son S, Ju S, Kim W, et al. Spectrally selective nanoparticle mixture coating for passive daytime radiative cooling. *ACS Appl Mater Interfaces* 2021;13(18):21119–26.
- Kim G, Park K, Hwang KJ, Jin S. Highly sunlight reflective and infrared semi-transparent nanomesh textiles. *ACS Nano* 2021;15(10):15962–71.
- Chae D, Kim M, Lim H, Lee D, Son S, Ha J, et al. Selectively emissive fluoropolymer film for passive daytime radiative cooling. *Opt Mater* 2022;128:112273.
- Zhang Y, Zhu W, Zhang C, Peoples J, Li X, Felicelli AL, et al. Atmospheric water harvesting by large-scale radiative cooling cellulose-based fabric. *Nano Lett* 2022;22(7):2618–26.
- Liu YR, Zhang HF, Zhang YH, Liang C, An Q. Rendering passive radiative cooling capability to cotton textile by an alginate/CaCO₃ coating via synergistic light manipulation and high water permeation. *Compos B Eng* 2022;240:109988.
- Wei W, Zhu Y, Li Q, Cheng ZF, Yao YJ, Zhao Q, et al. An Al₂O₃-cellulose acetate-coated textile for human body cooling. *Sol Energy Mater Sol Cells* 2020;211:110525.
- Ji Y, Sun Y, Muhammad J, Li X, Liu Z, Tu P, et al. Fabrication of hydrophobic multilayered fabric for passive daytime radiative cooling. *Mater Des* 2017;137(4):2100795.
- Shi NN, Tsai CC, Carter MJ, Mandal J, Overvig AC, Sfeir MY, et al. Nanostructured fibers as a versatile photonic platform: radiative cooling and waveguiding through transverse Anderson localization. *Light Sci Appl* 2018;7(1):37.
- Miao D, Cheng N, Wang X, Yu J, Ding B. Integration of janus wettability and heat conduction in hierarchically designed textiles for all-day personal radiative cooling. *Nano Lett* 2022;22(2):680–7.
- Hu R, Liu YD, Shin SM, Huang SY, Ren XC, Shu WC, et al. Emerging materials and strategies for personal thermal management. *Adv Energy Mater* 2020;10(17):1903921.
- Peng YC, Cui Y. Advanced textiles for personal thermal management and energy. *Joule* 2020;4(4):724–42.
- Cramer MN, Gagnon D, Laitano O, Crandall CG. Human temperature regulation under heat stress in health, disease, and injury. *Physiol Rev* 2022;102(4):1907–89.
- Zhai HT, Fan DS, Li Q. Dynamic radiation regulations for thermal comfort. *Nano Energy* 2022;100:107435.
- Liu XH, Wang DT, Yang ZW, Zhou H, Zhao QB, Fan TX. Bright silver brilliancy from irregular microstructures in butterfly culetis acuta moore. *Adv Opt Mater* 2019;7(18):1900687.
- Lou CH, An S, Yang RH, Zhu HR, Shen QC, Jiang MD, et al. Enhancement of infrared emissivity by the hierarchical microstructures from the wing scales of butterfly *Rapala dioetas*. *APL Photonics* 2021;6(3):036101.
- Shi NN, Tsai CC, Camino F, Bernard GD, Yu N, Wehner R. Keeping cool: enhanced optical reflection and radiative heat dissipation in Saharan silver ants. *Science* 2015;349(6245):298–301.
- Zhang H, Ly KCS, Liu X, Chen Z, Yan M, Wu Z, et al. Biologically inspired flexible photonic films for efficient passive radiative cooling. *Proc Natl Acad Sci USA* 2020;117(26):14657–66.
- Xie D, Yang Z, Liu X, Cui S, Zhou H, Fan T. Broadband omnidirectional light reflection and radiative heat dissipation in white beetles *Goliathus goliatus*. *Soft Matter* 2019;15(21):4294–300.
- Zheng XL, Yang QS, Hu YW, Lei CL, Wang XP. Latitudinal variation of morphological characteristics in the swallowtail *Sericinus montelus* Gray, 1798 (Lepidoptera: Papilionidae). *Acta Zool* 2015;96(2):242–52.
- Tsai CC, Childers RA, Nan Shi N, Ren C, Pelaez JN, Bernard GD, et al. Physical and behavioral adaptations to prevent overheating of the living wings of butterflies. *Nat Commun* 2020;11(1):551.
- Wang W, Yao Y, Luo T, Chen L, Lin J, Li L, et al. Deterministic reshaping of breath figure arrays by directional photomanipulation. *ACS Appl Mater Interfaces* 2017;9(4):4223.
- Liu W, Li C, Lin X, Xie H, Chen Y, Li Z, et al. Ordered porous films of biomass-based polymers by breath figure: a review. *Cellul* 2022;29:6463.